

9-2013

Molecular dynamics simulations of PMMA slabs: role of annealing conditions

Yae-ji Kim

Purdue University, kim758@purdue.edu

Keng-Hua Lin

Purdue University, lin105@purdue.edu

Alejandro Strachan

Birck Nanotechnology Center, Purdue University, strachan@purdue.edu

Follow this and additional works at: <http://docs.lib.purdue.edu/nanopub>



Part of the [Nanoscience and Nanotechnology Commons](#)

Kim, Yae-ji; Lin, Keng-Hua; and Strachan, Alejandro, "Molecular dynamics simulations of PMMA slabs: role of annealing conditions" (2013). *Birck and NCN Publications*. Paper 1461.

<http://dx.doi.org/10.1088/0965-0393/21/6/065010>

This document has been made available through Purdue e-Pubs, a service of the Purdue University Libraries. Please contact epubs@purdue.edu for additional information.

Molecular dynamics simulations of PMMA slabs: role of annealing conditions

This content has been downloaded from IOPscience. Please scroll down to see the full text.

2013 Modelling Simul. Mater. Sci. Eng. 21 065010

(<http://iopscience.iop.org/0965-0393/21/6/065010>)

View [the table of contents for this issue](#), or go to the [journal homepage](#) for more

Download details:

IP Address: 128.46.221.64

This content was downloaded on 07/11/2013 at 18:50

Please note that [terms and conditions apply](#).

Molecular dynamics simulations of PMMA slabs: role of annealing conditions

Yae-ji Kim, Keng-Hua Lin and Alejandro Strachan

School of Materials Engineering and Brick Nanotechnology Center, Purdue University,
West Lafayette, Indiana 47907, USA


Received 19 October 2012, in final form 31 May 2013

Published 24 July 2013

Online at stacks.iop.org/MSMSE/21/065010

Abstract

We use molecular dynamics simulations with the DREIDING force field to predict the molecular structure of thin PMMA slabs and characterize their properties. The slabs are created by uniaxial deformation of bulk samples at a high temperature followed by a relaxation and annealing to room temperature. Our simulations predict a free surface energy of $\sim 0.1 \text{ J m}^{-2}$ in good agreement with experimental measurements and a density away from the free surfaces similar to that of the bulk. We find that mechanical constraints during annealing affect the molecular structure of the slabs and their free surface energy; slabs composed of molecular chains elongated along the surface normal exhibit lower surface energies than those with isotropic chain structures.

 Online supplementary data available from stacks.iop.org/MSMSE/21/065010/mmedia

(Some figures may appear in colour only in the online journal)

1. Introduction

Understanding how specimen size and processing affect the thermo-mechanical response of amorphous polymers is critical to understand and, eventually, optimize nanocomposites and foams. These relatively new materials are interesting for a range of applications including nanoelectronics and electromagnetics, solar cells [1, 2], infrared sensors [3], electrolytes [4], microwave-absorbing and electromagnetic interference shielding [5, 6]. Good thermo-mechanical properties also open opportunities in automobile [7] and aerospace applications, coatings [8], flame retardants [9] and packaging [10].

The molecular structure of thin films present in nanocomposites and foams is likely to be different from those in bulk samples not only due to the presence of free surfaces and interfaces but also due to processing and thermal history [26, 27]. Understanding how these variables affect the molecular structure and, consequently, the properties of thin films would contribute to a more fundamental understanding of these materials.

Atomistic simulations play an increasingly important role in understanding the structure and physics of polymers. For example, molecular dynamics (MD) simulations provided insight into the role of size in the mechanical response of nanoscale polymer samples [11]

and contributed to the characterization of the heterogeneous distribution of local dynamic mechanical properties of glassy polymer thin films [12]. These simulations also helped in establishing firm relationships between molecular structure and properties; for example, polymer chain orientation effects on anisotropic plasticity [13] have been studied and so has the effect of entanglement density on strain hardening of polymer glasses [14]. While restricted to relatively small sizes and short timescales, these atomistic level simulations provide insight and quantitative information that can be used in continuum level models capable of achieving scales of interest in most real applications [28].

In this paper, we characterize the molecular structure, thermal properties and energetics of PMMA films obtained by drawing a bulk sample in the molten state and subsequently subjecting it to various thermal histories. The rest of the paper is organized as follows: computational details are included in section 2 and in section 3 we describe the generation of slabs and their annealing procedure. Results about structures and properties of PMMA slabs are covered in sections 4 and 5. Finally, discussion and conclusions are drawn in sections 6 and 7.

2. Computational details

All simulations use LAMMPS, a parallel MD simulation code from Sandia National Laboratories [15, 16]. The DREIDING force field [17] is used to describe the interaction between atoms in terms of covalent, van der Waals and electrostatic interactions. Partial atomic charges for electrostatics are obtained using the Gasteiger method [18]. We study two system sizes: (i) a small simulation cell containing five 96-monomer-long PMMA chains, leading to 7210 atoms and measuring approximately 4.13 nm on the side; and (ii) a larger cell with forty 96-monomer-long chains, with 57 680 atoms and 8.27 nm on the side. The initial bulk configurations were constructed at $T = 500$ K using the amorphous polymer builder of the commercial software MAPS [24]. All systems contain 80% of syndiotactic and 20% of atactic chains. These same structures were used previously to characterize the yield in PMMA under various loading conditions [23]. Similar structures can be built in the website with PolymerModeler [29]. Three-dimensional periodic boundary conditions are imposed on all systems. We use a time step of 4 fs to integrate the equations of motion with a RESPA multi-step algorithm that results in 1 fs updates for bond stretch, 2 fs for angles, dihedrals and improper forces and 4 fs for the van der Waals force and k -space calculations. As explained in section 3, slabs are created via deformation at high temperatures and the resulting systems are then annealed to room temperature. Temperature is adjusted with a Nose–Hoover thermostat with 0.4 ps coupling constant and pressure with a Nose–Hoover barostat with 4 ps coupling constant for the simulations. During this process a cutoff of 12.0 Å is used for non-bond interactions. A final thermalization using the more accurate but computationally more intensive particle–particle particle mesh (PPPM) solver with an accuracy of 10^{-4} kcal mol $^{-1}$ Å $^{-1}$ to handle long-range electrostatics is performed to quantify the effect of long-range interactions on free surface formation energy.

3. Generation of slabs and their annealing

This section describes the process used to create PMMA slabs via mechanical deformation. Section 3.1 describes the formation of slabs at high temperatures and their thermalization and section 3.2 describes the annealing of the samples.

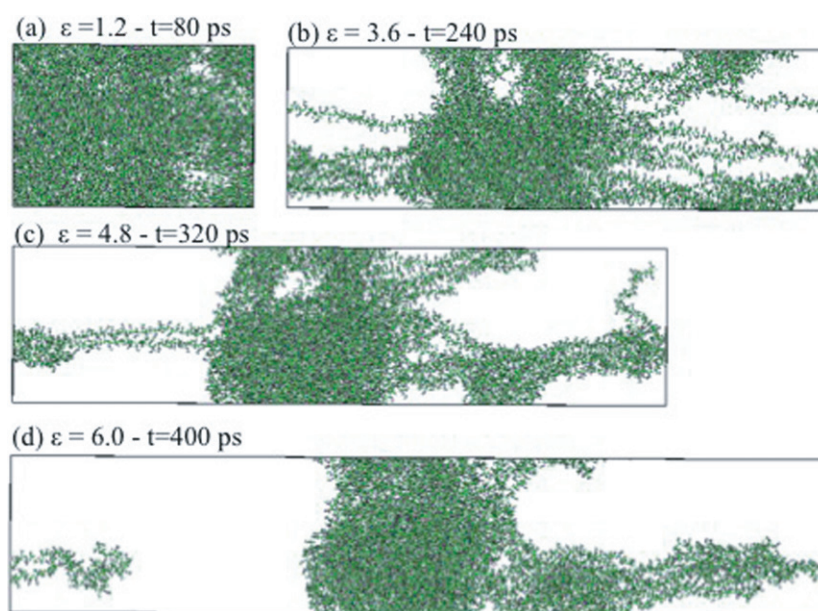


Figure 1. Atomic snapshots from the MD simulations used to create the PMMA slabs at various strain levels. Total deformation is 600% over a time of 400 ps.

3.1. Slab formation and relaxation

Deformation process. The periodic, bulk samples described above are thermalized at $T = 600$ K for 200 ps. The liquid samples are then uniaxially deformed along the z direction up to 600% engineering strain while keeping the cell lengths in the transverse directions constant. This deformation is done continuously (at every MD step) and with two different strain rates for the small system (7210 atoms): $1.45 \times 10^{10} \text{ s}^{-1}$ and $0.72 \times 10^{10} \text{ s}^{-1}$ and $0.72 \times 10^{10} \text{ s}^{-1}$ for the large system (57 680 atoms). The snapshots in figure 1 show the deformation process, including the nucleation and growth of voids and eventually the formation of a PMMA slab. The process of slab formation via mechanical deformation in the melt is akin to that used to synthesize polymer foams; see [21, 22] for polyimide foam synthesis from powder precursors.

The resulting structures are thermalized at $T = 600$ K for an additional time under constant volume and temperature conditions: 2400 ps for the large system, 400 ps for the small system deformed at $1.45 \times 10^{10} \text{ s}^{-1}$ strain rate and 800 ps for the small system at $0.72 \times 10^{10} \text{ s}^{-1}$. This time is enough for all polymer chains to coil back into a single slab and achieve an isotropic chain orientation distribution.

Figure 2 shows the longitudinal and transverse stresses as a function of strain during the deformation process. We see that for the fastest deformation rate the stress along the longitudinal direction is larger than the transverse one indicating that the liquid is not able to achieve mechanical equilibrium at such high rates. On the other hand, for the rate of $0.72 \times 10^{10} \text{ s}^{-1}$ the stress state of the system remains approximately hydrostatic throughout the simulation.

3.2. Slab annealing

After deformation and thermalization at $T = 600$ K the various structures are cooled down to room temperature. The systems are cooled down using two procedures: (i) isobaric, isothermal

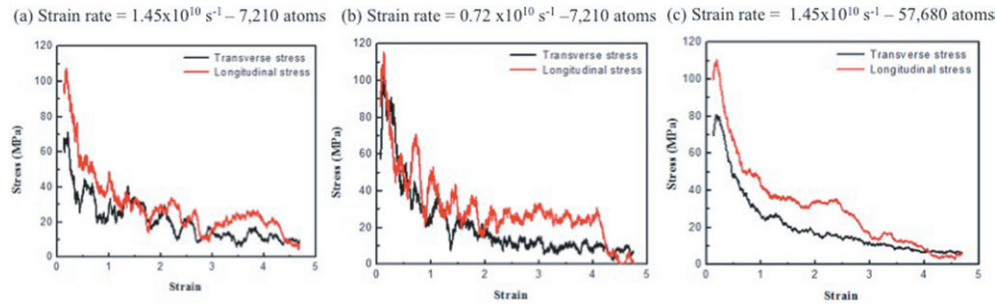


Figure 2. Stress–strain curves during deformation and thermalization.

Table 1. Thermo-mechanical history.

	Deformation at 600 K	Annealing from 600 to 300 K
Bulk 7210	X	NPT 25 K/100 ps NPT 10 K/200 ps
Slab 7210	Strain rate: $0.72 \times 10^{10} \text{ s}^{-1}$ Strain rate: $1.45 \times 10^{10} \text{ s}^{-1}$	NPT 25 K/100 ps NVT 10 K/200 ps
Bulk 57 680	X	NPT 25 K/100 ps NPT 10 K/200 ps
Slab 57 680	Strain rate: $1.45 \times 10^{10} \text{ s}^{-1}$	NPT 25 K/100 ps NVT 10 K/200 ps

MD (NPT ensemble) involving 25 K steps and 100 ps simulations at each temperature with zero stress along x and y directions (equal to the stress normal to the free surfaces) and (ii) isochoric, isothermal conditions (NVT) with a rate of 10 K every 200 ps. For comparison and to obtain surface energies, bulk systems (with 3D periodic boundary conditions) were also cooled down to room temperature using 25 K/100 ps and 10 K/200 ps rates under isobaric conditions. We performed an additional set of simulations to quantify the importance of long-range interactions during annealing. The slab and bulk systems with 57 680 atoms were cooled down from 600 to 300 K using the same NPT protocol with a cooling rate of 25 K/100 ps. In this case, long-range interactions are described using PPPM that provides an accurate description of long-range interactions. For the PPPM simulations we use a cutoff of 12 Å to separate short-range and long-range interactions and a convergence criterion of $10^{-4} \text{ kcal mol}^{-1} \text{ Å}^{-1}$ and a ‘slab’ correction as included in LAMMPS [15] to minimize dipole–dipole interactions across the periodic boundary normal to the slab surface. Table 1 summarizes the various models, and their thermo-mechanical history and structures are shown in figure 3.

The glass transition temperature of the bulk systems is characterized as 409 K with a cooling down of 20 K for every 100 ps to room temperature using NPT condition simulations. This prediction agreed with the experimental measurements of the a-PMMA T_g of 387 K and s-PMMA T_g of 404 K [25]. This provides an important validation of our molecular structures and the use of the DREIDING force field.

NPT cooling of slabs leads to a fast reduction of their cross-section above T_g as the liquid flows to minimize its free surface area. Figure 4 shows the transverse simulation cell parameters as a function of temperature for slabs and bulk systems. For both system sizes (7210 atoms and 57 680 atoms) the transverse cell length of the slab decreases approximately 30% when it is cooled down from 600 to 525 K by 25 K per 100 ps. In contrast, the slab cross-sectional area is held fixed during NVT annealing leading to a buildup of residual stress during cooling

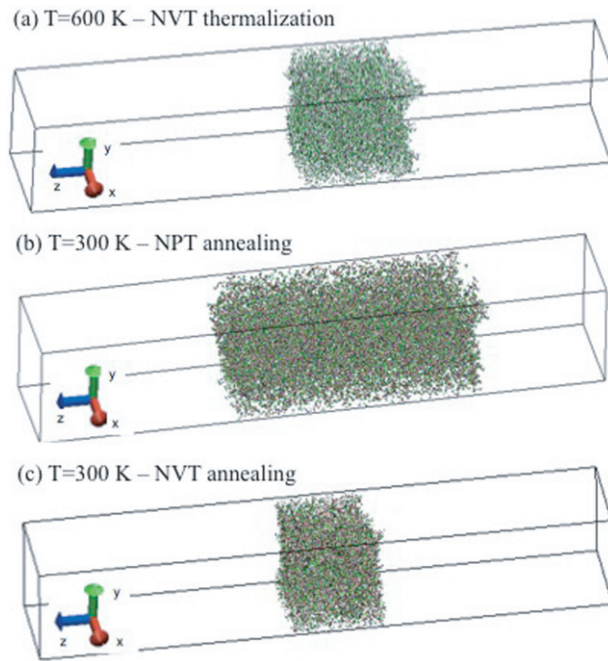


Figure 3. Atomistic snapshots of the PMMA slab (a) after deformation and thermalization at $T = 600$ K for 400 ps, and (b) after annealing to $T = 300$ K using NPT MD with a cooling rate of 25 K/100 ps, (c) after annealing to $T = 300$ K using NVT MD with a cooling rate of 10 K/200 ps.

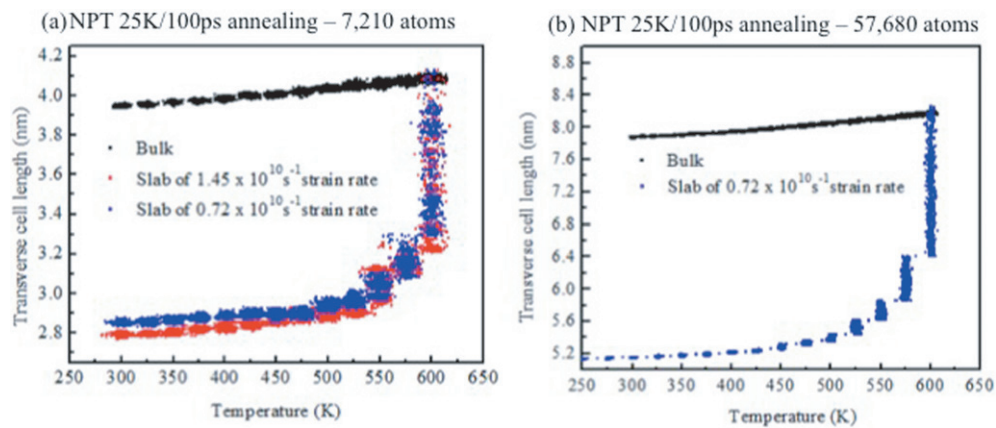


Figure 4. Transverse cell length change during annealing.

for temperatures below T_g . The annealing process affects the chain configurations in the solid, as will be discussed in section 4.

To further characterize the role of long-range electrostatic interactions in our predictions we performed a final thermalization of the $T = 300$ K slabs and bulk systems annealed using for both a 12 Å cutoff using PPPM, which provides an accurate treatment of the long-range Coulomb interactions. This final thermalization is 300 ps long.

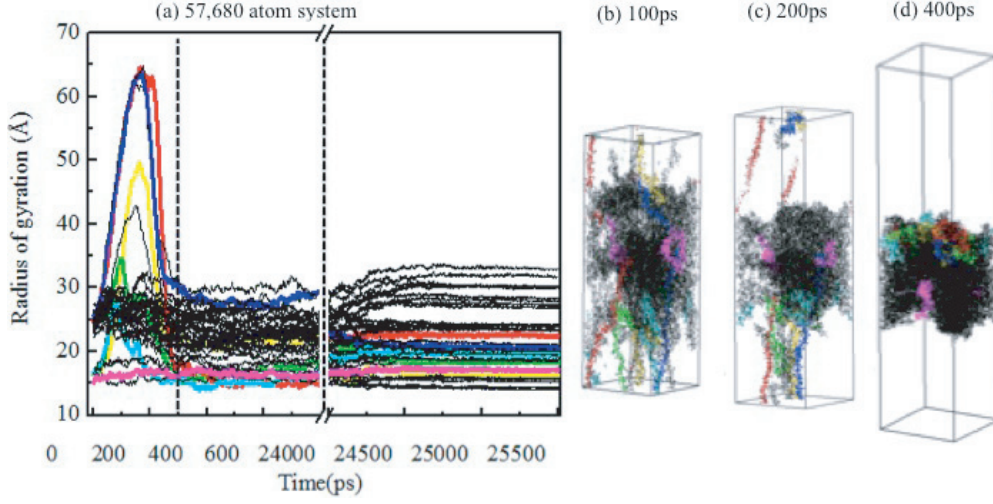


Figure 5. Radius of gyration while creating a PMMA slab and atomistic snapshots during deformation with six chains singled out.

4. Molecular structures

To characterize the polymer's molecular structure we study the distributions of radii of gyration during the formation and annealing of the films. The temporal evolution of the radius of gyration of every chain in the large system deformed with a strain rate of $1.45 \times 10^{10} \text{ s}^{-1}$ is shown in figure 5 during (i) deformation, (ii) thermalization at $T = 600 \text{ K}$ and (iii) annealing to room temperature (NPT with $25 \text{ K}/100 \text{ ps}$). We single out six chains to track the evolution of the radius of gyration during the process. Each color in the graph represents the individual chains of the same color in the snapshots in figures 5(b)–(d).

As expected, the chains with the largest increase in the radius of gyration are those located in the neck region during deformation. Those chains coil back when the slab forms and reduce their R_g . Interestingly, some of the chains with the largest increase in radius of gyration during deformation end up with very small radius in the slab as they finish coiled into themselves on the slab surface.

To better understand the molecular structure of the slabs we compute the radius of gyration normal to the free surface, defined as

$$R_{gZ} = \sqrt{\frac{3}{N} \sum_{i=1}^N (r_{iz} - r_{cz})^2} \quad (1)$$

and along the surface plane:

$$R_{gXY} = \sqrt{\frac{3}{2N} \left(\sum_{i=1}^N (r_{ix} - r_{cx})^2 + \sum_{i=1}^N (r_{iy} - r_{cy})^2 \right)} \quad (2)$$

where r_i is the position of atom i , r_c is the center of mass position of the chain and N is the number of atoms.

Figure 6 shows the distributions of R_{gZ} and R_{gXY} at various stages during the deformation and annealing process. The initial distributions before deformation are rather isotropic, figure 6(a), and R_{gZ} increases significantly during uniaxial deformation, see figure 6(b).

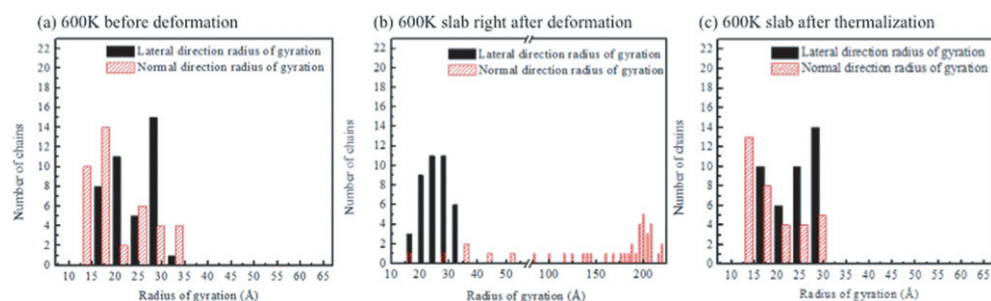


Figure 6. Radius of gyration of slabs and bulks at $T = 600$ K.

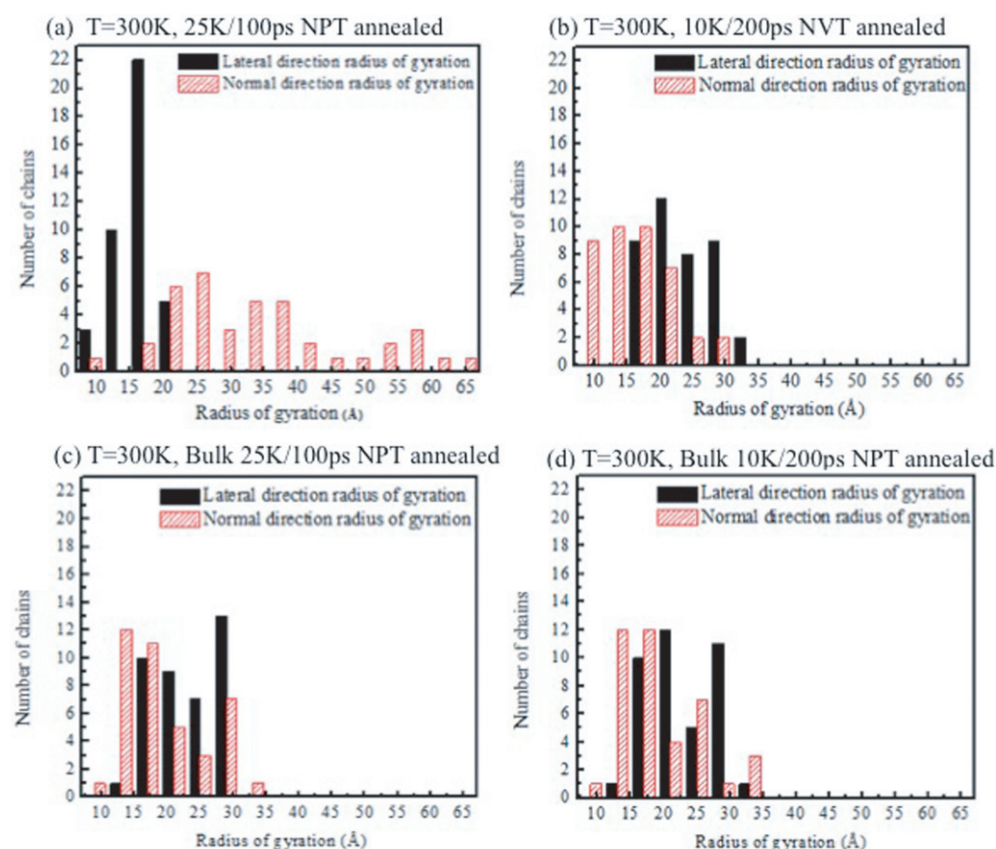


Figure 7. Radius of gyration of slabs and bulks at $T = 300$ K.

After the high-temperature thermalization following deformation R_{gZ} (normal to the surface) experiences a significant reduction as the highly elongated chains coil back and equilibrate. The transverse radius of gyration R_{gXY} remains rather constant throughout the entire process. As discussed earlier a slight reduction in the mean radius of gyration (about 4%) is observed during the deformation process.

Figures 7(a) and (b) show the distributions of radii of gyration after NPT and NVT annealing to room temperature. The resulting molecular structure after NPT cooling is highly

Table 2. Bond-orientational order parameter analysis.

	Before deformation	After deformation +2.4 ns thermalization	Slab at 300 K with NPT annealing	Slab at 300 K with NVT annealing	Bulk at 300 K
A	−0.021	−0.032	0.202	−0.045	0.0186

anisotropic. The reduction in the slab cross-section to minimize its free surface area leads to polymer chains elongated along the direction normal to the surface and becoming shorter in lateral directions. In contrast, the NVT-annealed slabs result in polymer chains elongated preferentially in the lateral direction rather than normal to the surface direction. These distributions resulting after the annealing procedure are rather stable within MD timescales and do not evolve significantly during the 300 ps long $T = 300$ K thermalization using a cutoff or the PPPM method. Figures 7(c) and (d) show the distribution of radii of gyration of bulk systems with different rates of annealing. In contrast with the slabs, their molecular structure does not show anisotropic distributions.

We also computed the bond-orientational order parameter to characterize the degree of alignment of polymer chains. Bond-orientational order parameter A is defined as

$$A = \frac{1}{n-2} \sum_{i=3}^{\kappa} \frac{3 \cos^2 \varphi_i - 1}{2} \quad (3)$$

where φ_i is the angle between the sub-bond vector $b_i - (r_i - r_{i-2})/2$ and the z -axis. The result of this analysis is shown in table 2.

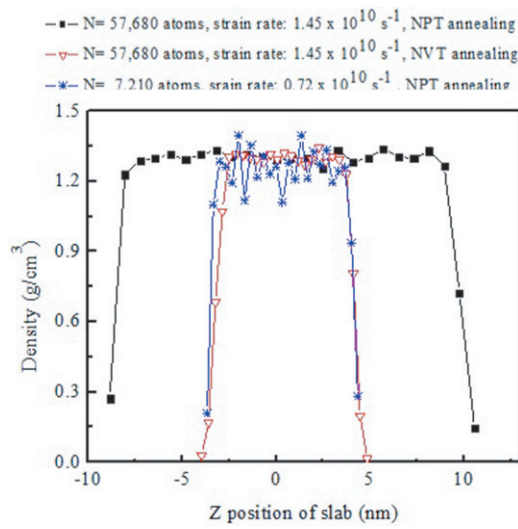
The parameter A represents the degree of alignment of polymer chains with the z -axis. Perfectly parallel chains would result in $A = 1.0$, random orientations in $A = 0.0$ and perpendicular to the z -axis would lead to $A = -0.5$. We see that 2.4 ns thermalization after deformation is enough time for the chains to achieve random orientations. Interestingly, slabs cooled down under constant stress show some degree of orientation in agreement with the radius of gyration analysis.

5. Slab properties

5.1. Density profiles

To analyze the density, we divide each simulation cell into 25 thin slabs (0.2–0.8 nm thick) and compute the density in each of them. Figure 8 shows the density profile of the slabs as a function of the z -axis after cooling and thermalization over 300 ps. Table 3 shows the density of each slab calculated from an average of 17 points in the center.

The annealing procedure has no appreciable effect on density despite the large change in molecular structures; we also find weak size dependence when we compare the density of different annealed slabs and different size slabs with larger slab density comparable to the bulk. Slabs annealed with NPT ensemble shrink in the in-plane direction to reduce their free surface area. The large system shrank by approximately 37% in width and the length of small systems shrank by about 29–31%. This surface area reduction leads to significantly different thicknesses in various structures depending on the annealing process. The thickness of the large NPT-annealed slab is approximately 2.2 times larger than the NVT-cooled slab; this ratio is in the range 1.73–1.83 for the small slabs. Dimensional information is organized in table 3. Despite the differences in processing and thickness NVT- and NPT-cooled small slabs exhibit

**Figure 8.** Density profiles of slabs.**Table 3.** Slab size and predicted properties.

	Length (nm)	Density (g cm ⁻³)	Surface energy (mJ m ⁻²)
Size: 7210 atoms	8.02	1.26 ± 0.09	50 ± 55
Strain rate: 0.72 × 10 ¹⁰ s ⁻¹			
Annealing: NPT 25 K/100 ps			
Size: 7210 atoms	8.38	1.25 ± 0.08	70 ± 60
Strain rate: 1.45 × 10 ¹⁰ s ⁻¹			
Annealing: NPT 25 K/100 ps			
Size: 7210 atoms	4.57	1.28 ± 0.10	80 ± 30
Strain rate: 0.72 × 10 ¹⁰ s ⁻¹			
Annealing: NVT 10 K/200 ps			
Size: 7210 atoms	4.65	1.26 ± 0.10	70 ± 30
Strain rate: 1.45 × 10 ¹⁰ s ⁻¹			
Annealing: NVT 10 K/200 ps			
Size: 57 680 atoms	19.44	1.31 ± 0.02	40 ± 20
Strain rate: 0.72 × 10 ¹⁰ s ⁻¹			
Annealing: NPT 25 K/100 ps			
Size: 57 680 atoms	8.81	1.30 ± 0.02	70 ± 20
Strain rate: 0.72 × 10 ¹⁰ s ⁻¹			
Annealing: NVT 10 K/200 ps			

similar densities: $1.26 \pm 0.10 \text{ g cm}^{-3}$. The large system cooled under NPT and NVT conditions also shows very different thickness but similar densities $1.31 \pm 0.02 \text{ g cm}^{-3}$. These values are similar to the bulk predictions of $1.29\text{--}1.30 \text{ g cm}^{-3}$. These results are slightly larger than the experimental value of 1.18 g cm^{-3} [19]. Thus, the density of the thin films is not noticeably affected by the mechanical constraints during the annealing of the films.

5.2. Surface energy

The surface energy of the various slabs is computed as

$$\gamma = \frac{\langle E_{\text{slab}} \rangle - \langle E_{\text{bulk}} \rangle}{2 \times \langle A \rangle} \quad (4)$$

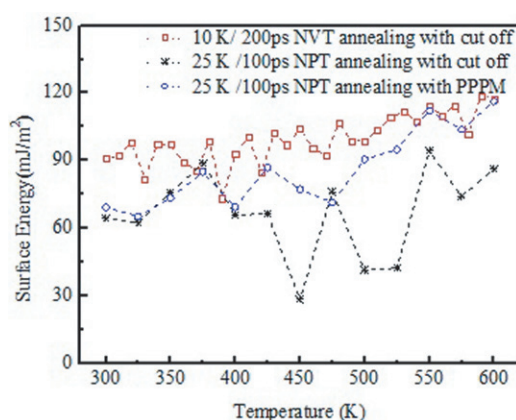


Figure 9. Surface energy versus temperature during annealing for slabs of 57 680 atoms with NPT 25 K/100 ps and NVT 10 K/200 ps annealing.

where E_{slab} and E_{bulk} are the total energy of the slab and bulk and A denotes the cross-sectional surface area of the simulation cell. Angle brackets indicate time average. The reference bulk energy corresponds to systems annealed at the same rate as the corresponding slab (but using NPT in all cases). As expected, the uncertainty in the calculated free surface energy, measured by its associated standard deviation, is large because it is obtained as the difference between two large numbers.

The predictions of surface energy as a function of temperature are shown in figure 9. We thermalized the 57 680-atom slab and bulk systems for an additional 200 ps for each temperature under NVT conditions for better statistics in the free surface energy calculation. Asterisks in figure 9 show the free surface energy as a function of temperature for large slabs cooled down under NPT conditions with a cutoff to describe electrostatics; diamonds show results for NPT cooling but with an accurate description of electrostatics using PPPM; finally, squares show results from NVT cooling. We observe a steep decrease in surface energy with decreasing temperature above the glass transition temperature for systems cooled down at a constant stress; below the glass transition temperature we observe a weak dependence of surface energy with temperature in the glass region. For slabs cooled under mechanical constraints (NVT) we predict a very gradual decrease in surface energy with decreasing temperature. The rapid decrease in surface energy coincides with the polymer flowing during cooling under constant stress conditions while mechanical constraint increases the energy of the slab, leading to a higher surface energy as compared with the NPT cases.

The Kirkwood–Buff equation [30, 31] provides an alternative approach to equation (4) to compute the surface tension of a liquid slab from normal and tangential stresses and we compare both approaches in the online supplementary material (stacks.iop.org/MSMSE/21/065010/mmedia). The Kirkwood–Buff surface energy values, obtained from NVT simulations, are slightly lower than those obtained using the energy difference approach (where the reference bulk systems are under zero stress) but otherwise show similar trends. A detailed analysis of the differences between the various methods used to compute surface energies for melts would be of interest but is beyond the scope of this paper where we focus on the resulting structure and properties of the resulting glass structures.

Table 3 summarizes our free surface energy predictions at 300 K from a 300 ps-long simulation averaging over the last 80 ps. Our results, ranging from 40 to 80 mJ m⁻², are in good agreement with experimental data: Ozcan and Hasirci reported the surface free energy

of PMMA by different approaches ranging from 30 mJ m^{-2} with the Berthelot method to $\sim 60 \text{ mJ m}^{-2}$ with the harmonic mean method [20]. As mentioned above, we find no systematic effect of deformation rate on surface energy; however, the mechanical constraints during annealing have a clear effect. Our results indicate that samples annealed under NPT conditions exhibit a lower free surface energy than those annealed while constraining their volume (NVT). As mentioned above, NPT-annealed slabs elongate along their normal directions and their chains do so as well. This causes the density of van der Waals bonds on the free surface to be smaller than in cases with isotropic chain conformations due to higher chain curvature and more chain ends near the surface.

6. Discussion

Our simulations show that the mechanical constraints during annealing affect the molecular structure of thin polymer films. The flow of liquid samples above T_g leads to an anisotropic distribution of the radius of gyration of the polymer chains. This information is relevant to the formation and annealing of polymer foams.

When polyimide foam samples are produced from poly(amic acid) (PAA) powder, the driving force for bubble growth initiation is the mechanical force associated with the pressure caused by the diffusion of the blowing agent into nuclei and is facilitated by the reduction in viscosity when the temperature reaches above the glass transition temperature of PAA. Thermal treatment around 150°C leads to an amidation reaction, which causes an increase in viscosity and bubble growth terminates [21, 22]. Thus, during foam formation and annealing the polymer experiences a thermo-mechanical history similar to those in our simulation and our results shed light on the possible structural changes induced by processing.

7. Conclusions

We used molecular dynamics simulations to create PMMA slabs by high-temperature uniaxial deformation followed by annealing to room temperature. We find that the conditions of the annealing process have a strong effect on the molecular structure of the resulting slabs. Slabs annealed with mechanical constraints exhibit isotropic molecular structures; in contrast, cases where surface tension drives a reduction in surface area lead to flow and anisotropic molecular structures. These molecular changes affect the free surface energies; we find structures with chains elongated normal to the slab surface to have lower surface energies. The free surface energy range predicted by the simulations is in good agreement with experimental measurements.

Acknowledgments

This work was supported by the US National Science Foundation, CMMI Grant 0826356 and by Purdue University. The authors gratefully acknowledge computational resources from nanoHUB.org and support from the Boeing Co.

References

- [1] Small C E, Chen S, Subbiah J, Amb C M, Tsang S-W, Lai T-H, Reynolds J R and So F 2012 *Nature Photon.* **6** 115–20
- [2] Oosterhout S D *et al* 2009 *Nature Mater.* **8** 818–24
- [3] Pradhan B, Setyowati K, Liu H, Waldeck D H and Chen J 2008 *Nano Lett.* **8** 1142–6

- [4] Tang C, Hackenberg K, Fu Q, Ajayan P M and Ardebili H 2012 *Nano Lett.* **12** 1152–6
- [5] Yang C, Li H, Xiong D and Cao Z 2009 *Reactive Funct. Polym.* **69** 137–44
- [6] Saini P, Choudhary V, Singh B P, Mathur R B and Dhawan S K 2009 *Mater. Chem. Phys.* **113** 919–26
- [7] Hussain F, Hojjati M, Okamoto M and Gorga R E 2006 *J. Compos. Mater.* **40** 1511–75
- [8] Sidorenko A, Ahn H-S, Kim D-I, Yang H and Tsukruk V V 2002 *Wear* **252** 946–55
- [9] Laoutid F, Bonnaud L, Alexandre M and Lopez-Cuesta J-M 2009 *Mater. Sci. Eng. R* **63** 100–25
- [10] Winey K I *et al* 2007 *MRS Bull.* **32** 314–22
- [11] Van Workum K and de Pablo J J 2003 *Nano Lett.* **3** 1405–10
- [12] Yoshimoto K, Jain T S, Nealey P F and de Pablo J J 2005 *J. Chem. Phys.* **122** 144712
- [13] Ge T and Robbins M O 2010 *J. Polym. Sci. B* **48** 1473–82
- [14] Hoy R S and Robbins M O 2006 *J. Polym. Sci. B* **44** 3487–500
- [15] LAMMPS (Large-scale Atomic/Molecular Massively Parallel Simulator) Open Source Code www.cs.sandia.gov/wsjpglmp/lammps.html
- [16] Plimpton S 1995 *J. Comput. Phys.* **117** 1–19
- [17] Mayo S L, Olafson B D and Goddard W A 1990 *J. Phys. Chem.* **94** 8897–909
- [18] Gasteiger J and Manili M 1980 *Tetrahedron* **36** 3219–88
- [19] Schmidt M and Maurer F H J 2000 *Macromolecules* **33** 3879–91
- [20] Ozcan C and Hasirci N 2008 *J. Appl. Polym. Sci.* **108** 438–46
- [21] Rocio Misiego C, Cano C I and Pipes B R 2009 *Polyimides and Other High-Temperature Polymers: Synthesis, Characterization and Application* vol 5, ed K L Mittal (Leiden: Koninklijke Brill NV) pp 307–21
- [22] Cano C I, Weiser E S, Kyu T and Pipes R B 2005 *Polymer* **46** 9296–303
- [23] Jaramillo E, Wilson N, Christensen S, Gosse J and Strachan A 2012 *Phys. Rev. B* **85** 024114
- [24] MAPS (The Materials and Processes Simulations platform) Scienomics Inc., 2008
- [25] Grohens Y, Brogly M, Labbe C, David M-O and Schultz J 1998 *Langmuir* **14** 2929–32
- [26] Li C and Strachan A 2011 *Polymer* **52** 2920–8
- [27] Lyulin A V and Michels M A J 2007 *Phys. Rev. Lett.* **99** 085504
- [28] Li C, Medvedev G A, Lee E-W, Kim J W, Caruthers J M and Strachan A 2012 *Polymer* **53** 4222–30
- [29] Haley B P, Li C, Wilson N, Jaramillo E and Strachan A 2013 *Comput. Phys. Commun.* submitted
- [30] Kirkwood J G and Buff F P 1949 *J. Chem. Phys.* **17** 338
- [31] in't Veld P J, Ismail A E and Grest G S 2007 *J. Chem. Phys.* **127** 144711